Steel and Composite Structures, *Vol. 36, No. 6* (*2020*) *671-687*
DOI: https://doi.org/10.12989/scs.2020.36.6.671

Bending and buckling analysis of sandwich Reddy beam considering shape memory alloy wires and porosity resting on Vlasov's foundation

Mostafa Bamdad[a], Mehdi Mohammadimehr* and Kazem Alambeigi[b]

Department of Solid Mechanics, Faculty of Mechanical Engineering, University of Kashan
P.O Box 87317-53153, Kashan, Iran

(*Received May 5, 2019, Revised July 12, 2020, Accepted July 15, 2020*)

Abstract. The aim of this research is to analyze buckling and bending behavior of a sandwich Reddy beam with porous core and composite face sheets reinforced by boron nitride nanotubes (BNNTs) and shape memory alloy (SMA) wires resting on Vlasov's foundation. To this end, first, displacement field's equations are written based on the higher-order shear deformation theory (HSDT). And also, to model the SMA wire properties, constitutive equation of Brinson is used. Then, by utilizing the principle of minimum potential energy, the governing equations are derived and also, Navier's analytical solution is applied to solve the governing equations of the sandwich beam. The effect of some important parameters such as SMA temperature, the volume fraction of SMA, the coefficient of porosity, different patterns of BNNTs and porous distributions on the behavior of buckling and bending of the sandwich beam are investigated. The obtained results show that when SMA wires are in martensite phase, the maximum deflection of the sandwich beam decreases and the critical buckling load increases significantly. Furthermore, the porosity coefficient plays an important role in the maximum deflection and the critical buckling load. It is concluded that increasing porosity coefficient, regardless of porous distribution, leads to an increase in the critical buckling load and a decrease in the maximum deflection of the sandwich beam.

Keywords: sandwich beam; Shape memory alloy; Buckling and bending; Porosity; Higher-order shear deformation theory; Vlasov's foundation

1. Introduction

In recent years, modern structures such as sandwich beams and new materials including SMA and porous materials have grabbed attention of the vast majority of researchers, meanwhile, many researchers focused on analyzing buckling and bending behaviors of sandwich beam, SMA and porous material (Arani *et al.* 2018, Babaee *et al*. 2018, Yazdani *et al*. 2019). Faraji-Oskouie *et al.* (2019) studied the bending behavior of small-scale Timoshenko beam based on the integral/differential nonlocal-micropolar elasticity theory. Their results illustrated that the nonlocal effect captured by the integral model is more outstanding than that in the differential model. Kaci *et al*. (2018) developed an exact analytical solution to analyze the post-buckling non-linear response of deformable symmetric composite beams. In their theory, they presented a parabolic distribution of transverse shear stresses in order to satisfy nullity conditions on both sides of the beam without the need of shear correction factor. Their results indicated that the classical and first-order theories underestimate the amplitude of buckling. Kozikowska (2019) studied topology and geometry optimization of statically determinate beams with arbitrary number of supports. He used Pareto optimality concept to formulate and solved the problem with the aim of minimizing the absolute maximum bending moment and the maximum deflection. Lee and Lee (2018) proposed a transfer matrix method for the bending vibration of two types of tapered beams subjected to axial force. They studied the effects of cracking and axial loading on behavior of the beam. Arani *et al.* (2019) used the nonlocal strain gradient elasticity theory and different higher order shear deformation beam theories simultaneously to study critical buckling load. They solved the governing equations by DQM and investigated the critical buckling load, critical voltage and critical temperature rising. The result demonstrated that with increasing the Winkler foundation, the buckling mechanical load is increased. Buckling and free vibration analysis of functionally graded sandwich I-beams based on the first-order shear deformation theory was studied by Nguyen *et al.* (2019). Their results indicated that the shear effects are more for beams with C-C boundary conditions, and are significant for beams with small span-to-height's ratio. Mohammadimehr and Rostami (2018) analyzed the static bending and vibration analysis of a rotating sandwich cylindrical shell with nanocomposite core and piezoelectric face sheets subjected to magnetic and thermal fields. They investigated the effect of geometrical parameters, applied voltages on the inner and outer piezoelectric layers and volume fractions of carbon nanotubes (CNT) on vibration behavior of sandwich cylindrical shell. They derived the governing equations of

*Corresponding author, Associate Professor
E-mail: mmohammadimehr@kashanu.ac.ir
[a]M.Sc.
[b] M.Sc.

ISSN: 1229-9367 (Print), 1598-6233 (Online)

motion from Lagrange's equations and used Ritz method to obtain the critical buckling loads and the natural frequencies of thin-walled beams for both non-shear deformable and shear deformable theory. Rajabi and Mohammadimehr (2019) investigated the bending analysis of a micro sandwich skew plate with isotropic core and piezoelectric composite face sheets based on the classical plate theory. Babaeeian and Mohammadimehr (2020) illustrated investigation of the time elapsed effect on residual stress measurement in a composite plate by DIC method.

Shape memory alloys represent a unique material class exhibiting peculiar properties such as the shape memory effect, the super-elasticity associated with damping capabilities, high corrosion and extraordinary fatigue resistance. The SMA, because of unique properties, is used in the wide fields of industry. For instance, in structural engineering and earthquake, because of super-elasticity and shape memory are used as wire, rod, and sheet to strengthen the structure against the earthquake. One of the most important applications of the SMA wires is orthodontic wires in dentistry. In recent years, many researchers have studied the stability and dynamic behaviors of sandwich beams embedded with SMA. Previous studies investigated the influence of SMA in mechanical behaviors of structures (He *et al.* 2017, Soltanieh *et al.* 2019, Yu *et al.* 2018). Kheirikhah and Khosravi (2018) studied the buckling and free vibration behaviors of the composite sandwich plates reinforced by SMA wires. The effects of geometry parameters like (thickness, plate aspect ratio) and boundary conditions on the natural frequencies and the critical buckling loads of the plates are investigated. The obtained results showed that an increase in the thickness ratio causes a decrease in both the dimensionless buckling load and the dimensionless natural frequency. Akhavan-Rad and Kheirikhah (2019) used third-order shear deformation plate theory to discuss the static analysis of a sandwich plate with flexible core and composite face sheets embedded with SMA wires in the face sheets. Their results showed that activating SMA wires causes a decrease in the deflection and stresses in these plates. Babaee *et al.* (2018) presented the nonlinear thermal buckling analysis of functionally graded (FG) beam integrated with shape memory alloy. They used the Brinson one-dimensional constitutive law to model the characteristics of SMA. Hamilton's principle is used to derive the nonlinear equilibrium equations. They studied the effect of material and geometrical parameters on the nonlinear thermal buckling. Kabir and Tehrani (2017) attempted to recognize the effects of SMA activation temperature, SMA fiber volume fraction, SMA pre-strain and biaxial ratio on the buckling and post-buckling solutions. Their results indicated that the active strain energy tuning (ASET) method is more effective than the active property tuning (APT) method in increasing the critical buckling load of the reinforced plates with SMA fibers. Akbari and Khalili (2019) examined numerically behavior of thin-walled composite shell with embedded SMA wires. They showed that the numerical model has sufficient accuracy on the buckling behavior of the composite structures embedded with SMA.

Porous materials are used in cases which the weight of structure plays a significant role. Because of this, exclusive properties have wide applications in biomedical, aerospace, automotive and civil engineering. Recently, researchers and engineers conducted many studies about various categories of porous materials such as organic materials, polymeric foams and metal foams (Thanh *et al.* 2019, Fang *et al.* 2019, Emdadi *et al*. 2019, Liu *et al*. 2019). Polit *et al.* (2019) analyzed the static bending and elastic stability of porous nanocomposite curved beams. Their results indicated that the weight dispersion pattern of GPLs significantly influences the stiffness of the beam while relating with the distribution of porosity in the metal foam. Tang *et al*. (2018) used Euler–Bernoulli beam theory and minimum total potential energy principle to derive the equilibrium equations. They analyzed the critical buckling load for different porosity distribution patterns by employing the generalized differential quadrature method (GDQM) to governing equations. Eltaher *et al.* (2018) studied the bending and vibration analysis of functionally graded (FG) nanobeams based on Euler beam theory (EBT). They solved equations by finite element method and showed that increasing porosity, material graduation and nanoscale parameters lead to decrease the bending resistance as well as the fundamental frequencies of the nanobeam. Their results showed that the static deflection increases with an increase in the porosity, nonlocal effect, and metal content into the material. Based on Hamilton's principle, Sahmani *et al*. (2018) extracted the non-classical governing differential equations of motion. Also, the influence of three different functionally graded porosity distributions and many other parameters is investigated. According to the presented results in mentioned study, among different patterns of porosity dispersion, the one that has higher Young's modulus in top and bottom of the beam provides minimum deflection of the beam. Alambeigi *et al*. (2020) presented free and forced vibration analysis of a sandwich beam considering porous core and SMA hybrid composite face layers on Vlasov's foundation. Amiri *et al.* (2020) considered stress and buckling analysis of a thick-walled micro sandwich panel with a flexible foam core and carbon nanotube reinforced composite (CNTRC) face sheets.

The focus of this research is to investigate the influence of temperature on bending and buckling behavior of the sandwich beam with porous core and composite face layers resting on Vlasov's foundation. As SMA wires which are embedded in composite face layers are significantly sensitive to temperature change. Moreover, the effect of some important parameter such as porosity coefficient, volume fractional of SMA, and volume fractional of BNNTs is studied. To the authors' best knowledge, this is for the first time that bending and buckling behavior of a sandwich beam with porous core and composite face layers embedded with SMA wires are studied. The porous core material is titanium alloy (Ti-6Al-4V) and the mechanical properties of porous core are assumed to be graded along the cross-section of the beam according to uniform and FG distribution patterns. The boundary conditions of the beam are supposed to be simply supported and the interface between the core and face layers are considered to be fully

bonded. In order to solve the governing equations Navier's solution is applied.

2. Layers formulation

2.1 Shape memory alloy

In this study, the used memory alloy is made of nickel-titanium and its phase is transformed with temperature. 1D Brinson model is used to simulate the modeling of memory alloy behavior. The fundamental equation of the SMA presented by Brinson is as follows Babaee *et al.* (2018)

$$\sigma - \sigma_0 = E(\xi)\varepsilon - E(\xi_0)\varepsilon_0 + \Omega(\xi)\xi_s - \Omega(\xi_0)\xi_{s0} + \theta(T - T_0) \quad (1)$$

At the above equation $\sigma, E, T, \Omega, \varepsilon, \theta$, and ξ_S illustrate stress, Young's modulus, temperature, phase transformation coefficient, strain, thermoelastic term, and martensite fraction induced by stress, respectively. Subscript 0 denotes the value at the onset of the current phase transformation.

The martensite phase volume fraction is defined by ξ. When $\xi = 0$, SMA is in the fully austenite phase and in the fully martensite phase $\xi = 1$.

$$\xi = \xi_S + \xi_T \quad (2)$$

In which, ξ_S and ξ_T demonstrate the martensite fraction induced by stress and the martensite fraction induced by temperature, respectively. It should be noticed that the effect of martensite fraction induced by temperature is studied in this research.

Based on the Brinson model Ω can be presented as follow

$$\Omega(\xi) = -\varepsilon_L E(\xi) \quad (3)$$

In which, ε_L is the maximum residual strain of SMA that can be calculated from experimental results.

By substituting Eq. (3) to the fundamental equation (Eq. (1)), generally Brinson model constitutive law can be written as follows

$$\sigma = E(\xi)(\varepsilon - \varepsilon_L \xi_s) + \theta(T - T_0) \quad (4)$$

The Young's modulus of SMA based on Reuss method is obtained Babaee *et al*. (2018)

$$E(\xi) = \frac{E_A}{1 + \left(\frac{E_A}{E_M} - 1\right)\xi} \quad (5)$$

In which, E_A and E_M represent the fully austenite and fully martensite modulus, respectively. The martensitic fraction at low temperature can be obtained by Brinson's model as the following
De-Sousa *et al*. (2018)

$$M_f < T < M_s$$

$$\xi_T = \frac{1 - \xi_0}{2}\left[\cos\left(\frac{\pi(T - M_f)}{M_s - M_f}\right) + 1\right] \quad (6)$$

In which, M_s and M_f depict the start and final temperature in martensite phase, respectively. At high temperature martensitic fraction is

$$A_s < T < A_f$$

$$\xi_T = \frac{\xi_0}{2}\left[\cos\left(\frac{\pi(T - A_s)}{A_f - A_s}\right) + 1\right] \quad (7)$$

2.2 Effective properties of composite layer

The Young's modulus of BNNT/epoxy composite is calculated by using the Halpin-Tsai equation as following Rafiee *et al.* (2009)

$$E_{\text{BNNT/epoxy}} = \frac{3}{8}\frac{1 + 2\left(\frac{l_{BNNT}}{d_{BNNT}}\right)\left(\frac{(E_{eq}/E_{epoxy}) - 1}{(E_{eq}/E_{epoxy}) + 2(l_{BNNT}/d_{BNNT})}\right)V^*}{1 - \left(\frac{(E_{eq}/E_{epoxy}) - 1}{(E_{eq}/E_{epoxy}) + 2(l_{BNNT}/d_{BNNT})}\right)V^*} \times E_{epoxy} + \frac{5}{8}\frac{1 + 2\left(\frac{(E_{eq}/E_{epoxy}) - 1}{(E_{eq}/E_{epoxy}) + 2}\right)V^*}{1 - \left(\frac{(E_{eq}/E_{epoxy}) - 1}{(E_{eq}/E_{epoxy}) + 2}\right)V^*} \times E_{epoxy}$$

$$E_{eq} = 4\left(\frac{t_{BNNT}}{d_{BNNT}}\right) \times E_{BNNT} \quad (8)$$

In which, V^* and E_{eq} are the volume fraction and the equivalent modulus of the boron nitride, respectively.

Three different distributions of BNNT along the z-direction are given in Appendix A. The Poisson's ratio and mass density for two phase of BNNT/epoxy resin are expressed as Mohammadimehr *et al.* (2018b)

$$\upsilon_{\text{BNNT/epoxy}} = V_{BNNT}\upsilon_{BNNT} + V_{epoxy}\upsilon_{epoxy}$$
$$\rho_{\text{BNNT/epoxy}} = V_{BNNT}\rho_{BNNT} + V_{epoxy}\rho_{epoxy} \quad (9)$$

The effective Young's modulus, Poisson's ratio and mass density of composite layer (SMA wires and BNNT/epoxy) are calculated by using the rule of mixture as follows

$$E_m = V_{SMA}E(\xi) + V_{\text{BNNT/epoxy}}\ E_{\text{BNNT/epoxy}}$$
$$\upsilon_m = V_{\text{SMA}}\upsilon_{SMA} + V_{\text{BNNT/epoxy}}\ \upsilon_{\text{BNNT/epoxy}}$$
$$\rho_m = V_{SMA}\rho_{SMA} + V_{\text{BNNT/epoxy}}\ \rho_{\text{BNNT/epoxy}} \quad (10)$$
$$V_{\text{BNNT/epoxy}} = 1 - V_{\text{SMA}}$$

In which, V_{SMA} is the volume fraction of SMA wires. Also, E_m, υ_m and ρ_m denote the effective Young's modulus, Poisson's ratio and mass density, respectively.

In Table 1, the mechanical properties of BNNTs and epoxy resin are given. In which, t, d and l represent the thickness, diameter and length of boron nitride nanotube (Mohammadimehr *et al.* 2018a, b, Arenal *et al.* 2011, Wu *et al*. 2015, Huang *et al.* 2011).

2.3 Porous core

In this part, the core is made of Ti-6Al-4V alloy foams and porosity is distributed through the thickness in different patterns. Thickness (z-direction in a Cartesian coordinate

Table 1 Geometry and mechanical properties of BNNT, epoxy resin and porous core

Properties	$E[Pa]$	ν	$\rho[\frac{Kg}{m^3}]$	$t_{BNNT}[m]$	$d_{BNNT}[m]$	$l_{BNNT}[m]$
BNNT	1.8×10^{12}	0.34	3487	0.07×10^{-9}	10×10^{-9}	30×10^{-9}
Epoxy resin	15.47×10^{9}	0.3	1100	-	-	-
Porous core	113.8×10^{9}	0.342	4430	-	-	-

system), width and length (x-direction in a Cartesian coordinate system) of the sandwich beam are shown via h, b and L, respectively.

The mechanical properties of core is graded in z-direction of coordinate system. The effective elastic modulus and mass density of porous core are written as follows Bamdad *et al*. (2019)

$$E_c(z) = E^*[1 - e_0\psi(z)] \qquad \rho_c(z) = \rho^*[\lambda(z)] \tag{11}$$

Where E^* and ρ^* denote Young's modulus and mass density when the core metal foam hasn't any porosity. e_0 represents the coefficient of porosity, $\psi(z)$ and $\lambda(z)$ refer to the three different porosity distributions which are chosen in this study as uniform, symmetric and asymmetric that are expressed in Appendix B. Also, $E_c(z)$ and $\rho_c(z)$ are the Young's modulus and density of core in which varies in z direction. The mechanical properties of porous core are given in Table 1 Chen *et al*. (2016).

The Poisson's ratio of FG porous cored is given as

$$\upsilon(z) = 0.221\left[1-\frac{\rho_c(z)}{\rho^*}\right] + \upsilon^*\left(0.342\left[1-\frac{\rho_c(z)}{\rho^*}\right]^2 - 1.21\left[1-\frac{\rho_c(z)}{\rho^*}\right]+1\right) \tag{12}$$

3. Theory and governing equations

3.1 Displacement field

A sandwich Reddy beam with FG core and SMA wires embedded composite face sheets has been considered in this research. Reddy beam theory (RBT) is used as following AkhavanAlavi *et al.* (2019), Wattanasakulpong and Bui (2018)

$$u^i(x,z) = u_0^i(x) + z\emptyset^i(x) - \frac{4z^3}{3h_i^2}\left(\emptyset^i(x) + \frac{dw_0^i(x)}{dx}\right) \qquad w^i(x,z) = w_0^i(x) \quad , \quad i = core \ \& \ face\ sheets \tag{13}$$

In which, u and w are displacement components of an arbitrary point along the x and z axes, respectively, and $\emptyset$ denotes the rotation about the y-axis. Besides, u_0 and w_0 demonstrate the displacement components on the middle surface of beam in the x and z directions according to Fig. 1. The strain components of RBT is derived from the displacement field are shown in Appendix C.

3.2 Constitutive equations

Based on the elasticity theory, the constitutive equations of SMA/FG smart composite sandwich beam that is undergone thermal loading are given as follows Babaee *et al.* (2018)

$$\sigma_{xx} = \begin{cases} Q_{11}\varepsilon_{xx} + E(\xi)\xi_S\varepsilon_L + \Theta(T-T_0) \\ (composite\ layers\ embedded\ with\ SMA) \\ C_{11}\varepsilon_{xx} \\ (FG\ core) \end{cases} \qquad \tau_{xz} = \begin{cases} Q_{55}\gamma_{xz} \\ (composite\ layers\ embedded\ with\ SMA) \\ C_{55}\gamma_{xz} \\ (FG\ core) \end{cases} \tag{14}$$

In which Q and C are elastic stiffness that are defined in Appendix D. ε_{xx} and γ_{xz} are the normal and shear strains, respectively. σ_{xx} and τ_{xz} denote the normal and shear strains, respectively.

3.3 External work

In this study, the principle of virtual work is used to obtain the maximum deflection by applying the actual transverse force and also, to acquire the critical buckling load for a simply supported beam. The variation of external work is defined as follows (Wang *et al*. 2000)

$$W_{ext} = -\frac{1}{2}\int_0^l\left(N_x\left(\frac{dw_0}{dx}\right)^2 + qw_0\right)dx \qquad \delta W_{ext} = -\int_0^l\left(q + N_x\frac{d^2w_0}{dx^2}\right)\delta w_0 dx \tag{15}$$

In which, N_x and q denotes the axial force along the length of the beam and transverse distributed load at the top surface of the beam, respectively. W_{ext} is the work done by the external loads.

3.4 Strain energy

The variation of strain energy for SMA/FG smart composite sandwich beam can be calculated as follows

$$U_s = \frac{1}{2}\int_{Core}(\sigma_{xx}\varepsilon_{xx} + \tau_{xz}\gamma_{xz})dV + \frac{1}{2}\int_{upper\ sheet}(\sigma_{xx}\varepsilon_{xx} + \tau_{xz}\gamma_{xz})dV + \frac{1}{2}\int_{lower\ sheet}(\sigma_{xx}\varepsilon_{xx} + \tau_{xz}\gamma_{xz})dV$$

$$\delta U_s = \int_{Core}(\sigma_{xx}\delta\varepsilon_{xx} + \tau_{xz}\delta\gamma_{xz})dV + \frac{1}{2}\int_{upper\ sheet}(\sigma_{xx}\delta\varepsilon_{xx} + \tau_{xz}\delta\gamma_{xz})dV + \frac{1}{2}\int_{lower\ sheet}(\sigma_{xx}\delta\varepsilon_{xx} + \tau_{xz}\delta\gamma_{xz})dV \tag{16}$$

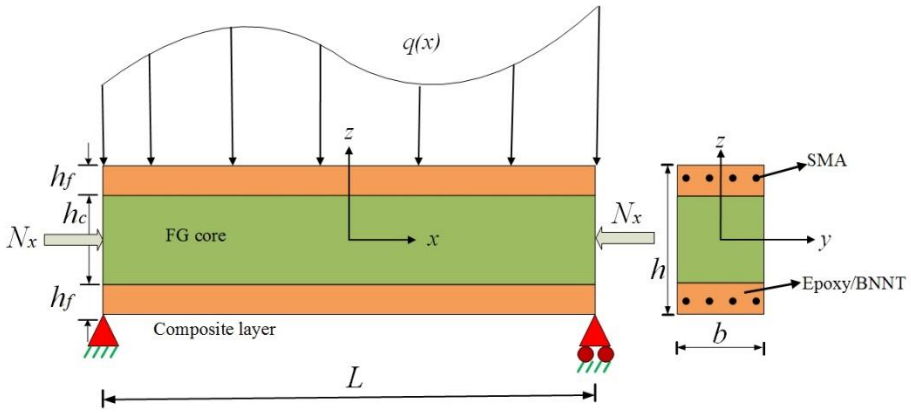

Fig. 1 Schematic of sandwich beam with porous core and composite face layers

Where U_s is the strain energy due to the mechanical loads.

The displacement field of Vlasov's model foundation is supposed as follows (Arenal *et al.* 2011)

$$u_f(x,z) = 0$$
$$w_f(x,z) = w_0(x)\chi(z) \tag{17}$$

According to this model, there is no horizontal displacement, $w_0(x)$ and $\chi(z)$ are indicate vertical displacement of mid surface and shape function of foundation, respectively. Boundary conditions for shape function as follows

$$\chi\left(-\frac{h_c}{2} - h_f\right) = 1, \qquad \chi\left(-\frac{h_c}{2} - h_f - H\right) = 0 \tag{18}$$

In which, H is the thickness of the foundation. Using the strain-displacement equations of elasticity, the strain components can be expressed as

$$f_{\varepsilon_{xx}} = 0$$
$$f_{\varepsilon_{zz}} = w_0(x)\frac{d\chi(z)}{dz} \tag{19}$$
$$f_{\gamma_{xz}} = \chi(z)\frac{dw_0(x)}{dx}$$

The constitutive equations for the isotropic foundation can be expressed as follows

$$\begin{Bmatrix}\sigma_{xx}\\ \sigma_{zz}\\ \tau_{xz}\end{Bmatrix}^f = \begin{bmatrix}D_{11} & D_{12} & 0\\ D_{21} & D_{11} & 0\\ 0 & 0 & D_{55}\end{bmatrix}^f \begin{Bmatrix}0\\ \varepsilon_{zz}\\ \gamma_{xz}\end{Bmatrix}^f \tag{20}$$

In which, D is the elastic stiffness of the foundation that is defined in Appendix E. The strain energy of Vlasov's foundation can be derived as follows

$$\mathrm{U}_f = \frac{1}{2}\int_f (\sigma_{zz}\varepsilon_{zz} + \tau_{xz}\gamma_{xz})dV$$
$$\delta\mathrm{U}_f = \int_f (\sigma_{zz}\delta\varepsilon_{zz} + \tau_{xz}\delta\gamma_{xz})dV \tag{21}$$

where U_f is the strain energy of Vlasov's foundation.

3.5 Principle of minimum total potential energy

By applying the principle of minimum total potential energy, the governing equations of Reddy beam subjected to the thermal loading are derived as (Ebrahimi and Barati 2018, Heydari and Shariati 2018)

$$\delta\Pi = \delta U + \delta W = 0 \tag{23}$$

Where δ denote the variation operator, U and W are the strain energy and external work, respectively. The governing equations are presented in Appendix F.

4. Numerical results

4.1 Solution method

In order to determine the critical buckling load and maximum deflection of the sandwich Reddy beam including porous cored and composite layers embedded with SMA wires, the analytical solution of Navier is utilized in this research (Chaabane *et al*. 2019):

$$u(x) = \sum_{n=1}^{\infty} U_n \cos\left(\frac{n\pi}{l}x\right)$$
$$w(x) = \sum_{n=1}^{\infty} W_n \sin\left(\frac{n\pi}{l}x\right) \tag{23}$$
$$\emptyset(x) = \sum_{n=1}^{\infty} \Phi_n \cos\left(\frac{n\pi}{l}x\right)$$

In which U_n, W_n and Φ_n are unknown maximum displacement coefficients. The transverse distributed load based on the Fourier series is expanded as follows (Thai and Vo 2012)

$$q(x) = \sum_{n=1}^{\infty} Q_n \sin\frac{n\pi}{L}x \tag{24}$$

Table 2 Comparison of dimensionless maximum deflection Arani *et al*. (2018))

Models	L/h		
	10	20	100
EBT*(Reference)	*1.3130*	*1.3130*	*1.3130*
Error percentage** (%)	*2*	0.3	*0.2*
TBT*(Reference)	1.3483	1.3155	1.3074
Error percentage (%)	0.2	0.2	0.1
RBT(present)	1.3454	1.3178	1.3100

** Euler-Bernoulli beam theory (EBT) & Timoshenko beam theory (TBT)*

** $Error\ percentage = \left|\frac{Ref-Pre}{REf}\right| \times 100$

Table 3 Comparison the dimensionless critical buckling load for simply supported boundary condition ofa san dwich beam between the preset work and Wu *et al.* (2015)

L/h	CNT Dist.	$V_{CNT} = 0.12$		$V_{CNT} = 0.17$		$V_{CNT} = 0.28$	
		present	*Wu et al.* (2015)	present	*Wu et al.* (2015)	present	*Wu et al.* (2015)
10	*UD*	*0.0068*	*0.0070*	*0.0081*	*0.0082*	*0.0104*	*0.0107*
	FG	*0.0070*	*0.0072*	*0.0084*	*0.0085*	*0.0109*	*0.0111*
20	*UD*	*0.0019*	*0.0018*	*0.0021*	*0.0021*	*0.0027*	*0.0028*
	FG	*0.0019*	*0.0018*	*0.0022*	*0.0022*	*0.0028*	*0.0029*
30	*UD*	*0.0008*	*0.0008*	*0.0009*	*0.0009*	*0.0011*	*0.0012*
	FG	*0.0008*	*0.0008*	*0.0010*	*0.0010*	*0.0012*	*0.0013*

In which, $Q_n = {}^{4q_0}/_{n\pi}$ is the amplitude for uniform load. It is noticeable that to obtain the critical buckling load, q is set to zero.

By solving the following system bending behavior of sandwich beam is obtained as

$$[K]\{\boldsymbol{R}\} = \{\boldsymbol{F}\} \tag{25}$$

In which K is the global stiffness matrix. The unknown vector $\boldsymbol{R}$ and the force vector $\boldsymbol{F}$ are defined as follows

$$\boldsymbol{R} = \{U_n \quad W_n \quad \Phi_n \ \}^T \tag{26}$$

$$\boldsymbol{F} = \{0 \quad \mathrm{q(x)} \quad 0 \ \}^T \tag{27}$$

To obtain the critical buckling load, the determinant of coefficients matrix of the following system should be equal to zero

$$\big([K] - N_x[K_g]\big)\{\boldsymbol{R}\} = \{\boldsymbol{0}\} \tag{28}$$

In which, N_x and K_g are the critical buckling load and the geometric stiffness, respectively.

4.2 Validation

As no published results for the SMA/FG smart composite sandwich Reddy beam under current consideration are available in open literature, bending analysis is validated with Arani *et al*. (2018). Table 2 is illustrated for ensuring the accuracy of results. And also, comparison of dimensionless maximum deflection [$\overline{w} = w * 10^2(EI/q_0L^4)$] in simply supported beams subjected to uniform load q_0 has been demonstrated.

($b = 1.1\ [m],\ L = 10\ [m],\ q_0 = 1\ [\frac{N}{m}],\ E = 30 \times 10^6[Pa],\ \upsilon = 0.3, I = \frac{1}{12}bh^3[m^4]$)

To validate the buckling analysis, the obtained results are compared with a sandwich beam with below properties. In Table 3, the comparison between the present work and the obtained results by Wu *et al.* (2015) is shown.

Poly methyl methacrylate (PMMA) is considered as matrix:

$$E_{PMMA} = 2.5 \times 10^9\ [Pa], \rho_{PMMA} = 1190[Kg/m^3], \nu_{PMMA} = 0.3$$

Carbon nanotube (CNT) is selected as reinforcement:

$$E_{CNT} = 5.6466 \times 10^{12}[Pa], \rho_{CNT} = 1400[Kg/m^3], \nu_{CNT} = 0.175$$

$$\eta_1 = \begin{cases} 0.137 & for\ V_{CNT} = 0.12 \\ 0.142 & for\ V_{CNT} = 0.17 \\ 0.141 & for\ V_{CNT} = 0.28 \end{cases}$$

In which, η_1 is the CNT efficiency parameter.

5. Results and discussion

In this research, the geometry parameters of the sandwich beam are assumed as follows

$${h_c}/{h_f} = 8\ , b = 0.5[m], h = 0.2[m], E^* = 113.8 \times 10^9[Pa], \upsilon^* = 0.342, \rho^* = 4430[Kgm^{-3}]$$

Table 4 Thermomechanical properties of NiTi SMA Babaee *et al.* (2018)

Modulus and density	Phase transformation temperature	Other parameters
$E_A = 67$ [GPa]	$A_s = 34.5$[℃]	$\nu_s = 0.33$
$E_M = 26.3$ [GPa]	$A_f = 49$ [°C]	$\varepsilon_L = 0.067$
$\theta = 0.55$[MPa°C^{-1}]	$M_s = 18.4$ [°C]	$T_0 = 25$[°C]
$\rho = 6450$ [Kg/m^3]	$M_f = 9$ [°C]	-

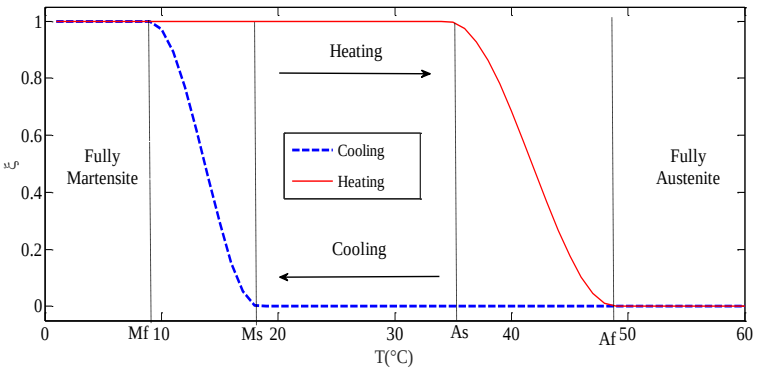

(a)

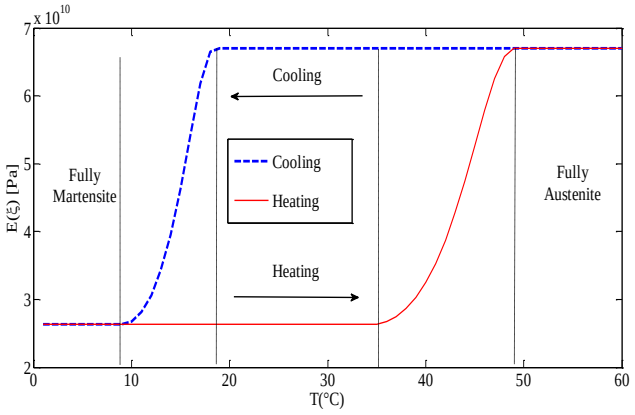

(b)

Fig. 2 (a) Process of changing the martensite volume fraction for a heating/cooling cycle of an SMA element and (b) the SMA Young's modulus behavior when it changes between two phases of fully austenite and fully martensite

In which, h_c and h_f describe the core and face sheet thicknesses, respectively. And also E^*, υ^* and ρ^*illustrates the pure Young's modulus, Poisson's ratio and density of porous core, respectively. The material properties of SMA are given in Table 4.

Based on the following dimensionless relations the results are obtained:

- **Bending :** → dimensionless maximum deflection

$$W_{max} = w \times 10^2\left(\frac{E^* I}{q_0 L^4}\right)] \quad , \quad I = \frac{1}{12} b h^3 [m^4]$$

- **Buckling** : → dimensionless critical buckling load

$$P_{cr} = N_x \frac{L^2}{E^* I}$$

5.1 Thermo-mechanical behaviour of SMA

By increasing the temperature from A_s to A_f, the phase transformation of martensite to austenite occurs. As indicated in Fig. 2, SMA wires in the austenite phase, have higher Young's modulus because of regular molecular shape and vice versa, by decreasing the temperature and transforming to the martensite phase, its molecular shape changes to irregular.

5.2 Influence of SMA and dispersion of porosity

In the study of buckling and bending, the most important parameters to be analyzed are the critical buckling load and maximum deflection, respectively.

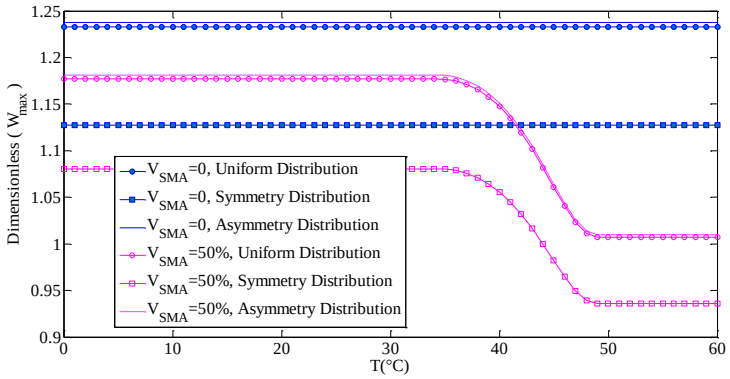

(a)

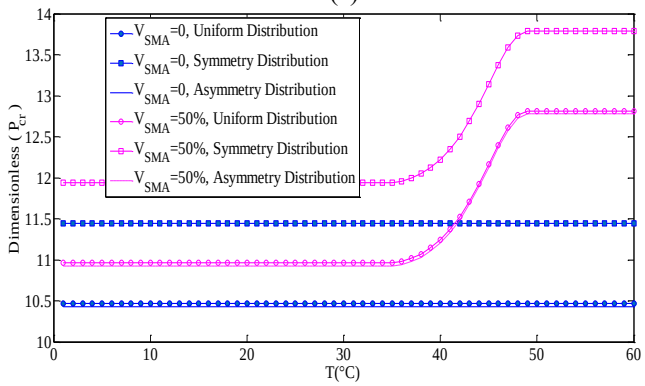

(b)

Fig. 3 Influence of SMA wires and dispersion of porosity on (a) dimensionless maximum deflection (b) dimensionless critical buckling load

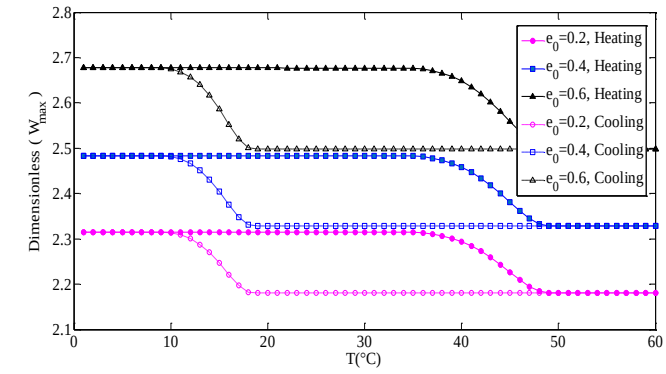

(a)

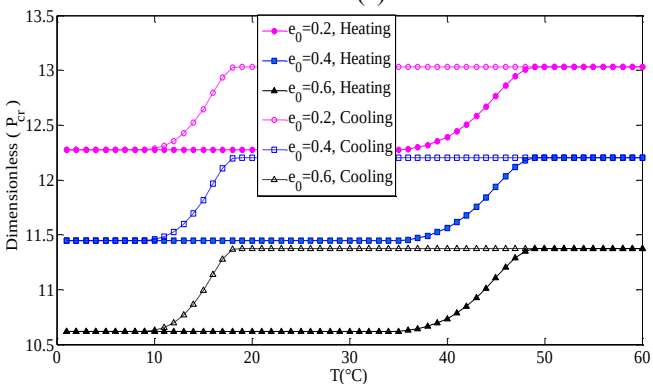

(b)

Fig. 4 The effect of porosity coefficient in a heating/cooling cycle of SMA wires on (a) dimensionless maximum deflection and (b) dimensionless critical buckling load

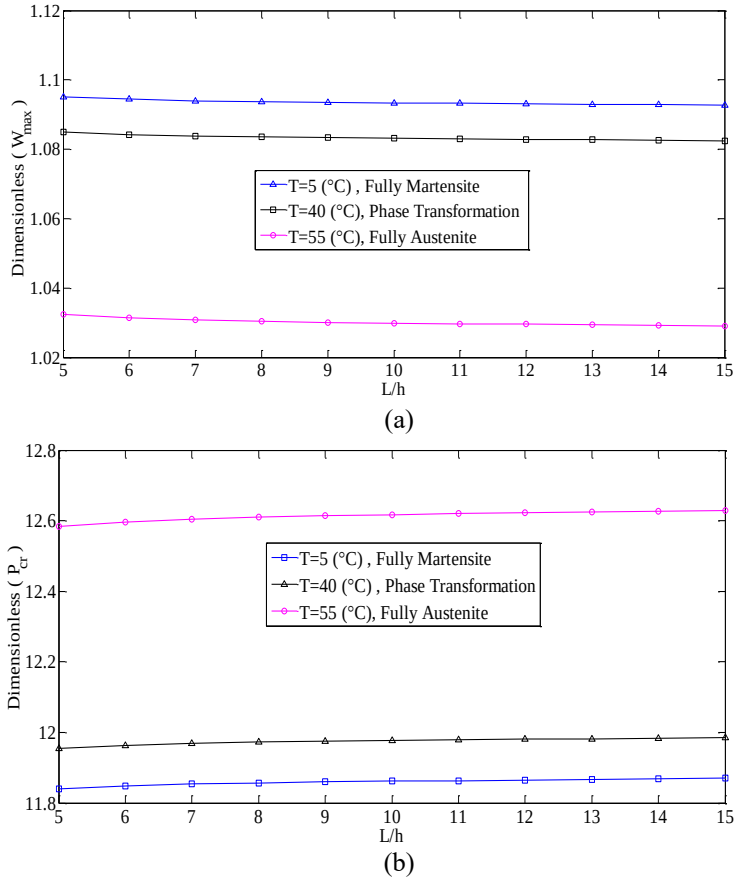

Fig. 5 Investigating the length to thickness ratio in the various phases (a) dimensionless maximum deflection (b) dimensionless critical buckling load

As shown in Fig. 3, when the beam is devoid SMA, the structure has weaker stiffness. And also by increasing the SMA temperature from A_s to A_f, the elastic modulus of SMA wires increases. Three different distributions of porosity are considered that the symmetry dispersion has more significant effect on the stiffness of the beam than the two other types of distribution. The maximum deflection and critical buckling load in term of T are presented in Fig. 3, for $e_0 = 0.3, W_{BNNT} = 2\%$ and uniform dispersion of BNNT.

5.3 Effect of porosity coefficient

For further study, the sensitivity of the structural response to the porosity coefficient in a heating/cooling cycle of SMA is calculated. Fig. 4 shows the influence of porosity coefficient on the buckling and bending behavior while the sandwich beam resting on the elastic foundation based on Vlasov's model, the thickness and density of foundation are considered $H = 0.5[m], \rho = 600[\frac{Kg}{m^3}]$ respectively.

5.4 Effect of length-to-thickness ratio and phase regions

The deflection and critical buckling load can be affected significantly by region of the phases, which variation is plotted in Fig. 5. As can be seen, region of fully austenite provides the highest amount of stiffness for the beam and region of fully martensite causes lowest quantity of stiffness for the sandwich beam. The symmetry distribution of porosity, $e_0 = 0.3, q_0 = 1\left[\frac{N}{m}\right], W_{BNNT} = 2\%, V_{SMA} = 0.2$ Vlasov's foundation and martensite fraction for a heating cycle of SMA are considered.

5.5 Influence of weight fraction of BNNTs

One of the effective parameters on critical buckling load and deflection is the weight fraction of BNNT. As shown in Fig. 6, by increasing the amount of boron nitride nanotube, the stiffness of the sandwich beam increases to some extent. While symmetry pattern is chosen as distribution of porosity and the beam is rest on Vlasov's foundation. This comparison is done between two regions (fully austenite & fully martensite).

5.6 Effect of volume fraction of SMA and different BNNTs patterns

The presented analysis in this section is delivered for the volume fraction of SMA and various patterns of BNNT. Fig. 7 illustrates that the type of A-V pattern has the lowest

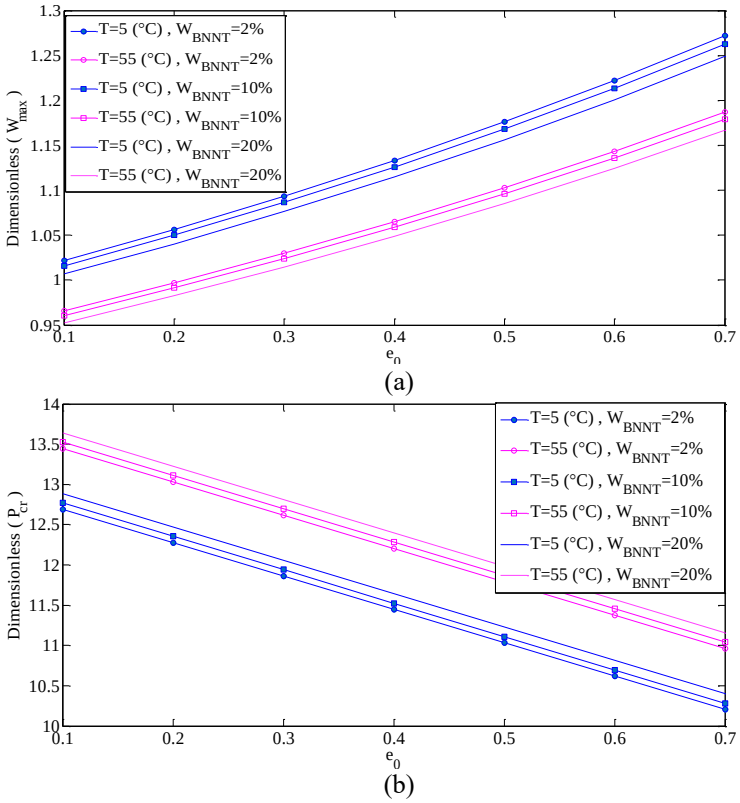

Fig. 6 Influence of weight fraction of BNNTs in different phases on (a) dimensionless maximum deflection (b) dimensionless critical buckling load. ($V_{SMA} = 0.2, e_0 = 0.3$)

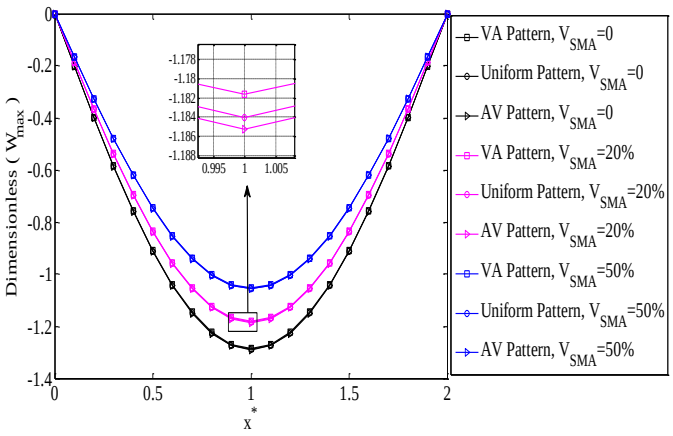

Fig. 7 Dimensionless maximum deflection in term of length of beam for different Patterns of BNNTs and volume fraction of SMA

stiffness and the highest stiffness belongs to V-A type. As can be seen the SMA volume fraction has a significant effect on the dimensionless maximum deflection of the sandwich beam. While the thickness of face sheets is equal to $h_f = 10[cm]$, the amount of weight fraction is $W_{BNNT} = 20\%$ and symmetry dispersion is considered as porosity distribution.

5.7 Effect of temperature changing

Comparison of the critical buckling load and deflection for different volume fractions of SMA in term of temperature are illustrated in Fig. 8. As shown in this figure, in the higher V_{SMA}, the rate of stiffness changes with temperature is more intensive. Moreover, by increasing the volume fraction of SMA, the size of the heating/cooling cycle is increased, which means the structure is more sensitive to variation of temperature. Porosity coefficient ($e_0 = 0.3$), the weight fraction of BNNT ($W_{BNNT} = 2\%$) and the symmetric distribution of pores are considered for this analysis.

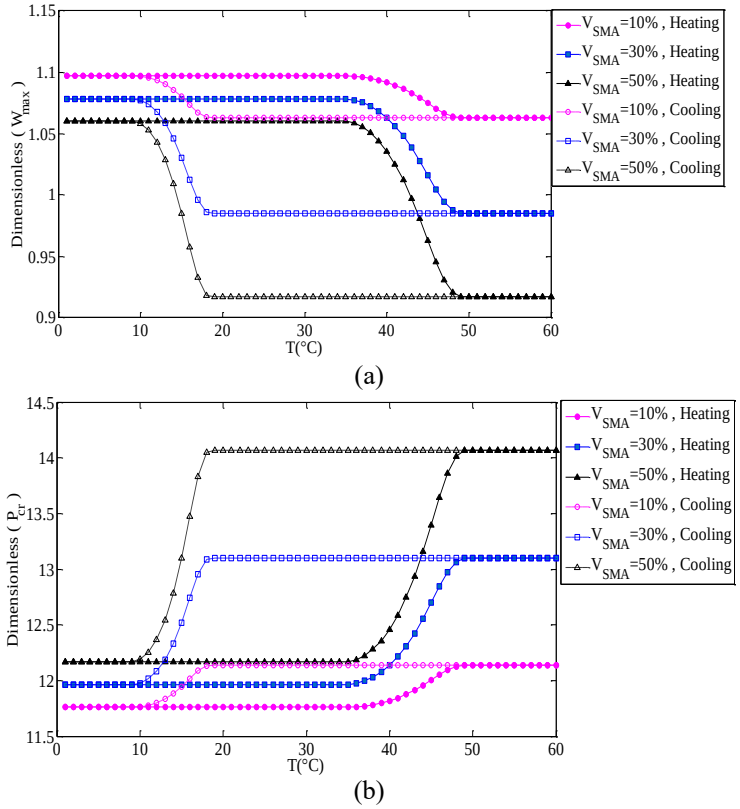

Fig. 8 Effect of SMA volume fraction in the heating/cooling temperature cycle on (a) dimensionless maximum deflection and (b) dimensionless critical buckling load

6. Conclusions

In this paper, the buckling and bending analysis of a sandwich beam with FG porous core and composite face sheets embedded with SMA wires are analytically investigated using the Navier method. By applying the third-order shear deformation theory and principle of minimum total potential energy, the governing equations are derived. The influence of three different patterns of BNNTs and also the three different distributions of porosity on the behavior of buckling and bending are studied. To obtain the effective properties of composite layers, Halpin-Tsai and rule of mixture are used. In addition, the influence of geometric parameters and effective parameters such as volume fraction of SMA, temperature, the thickness ratio of the beam, distribution of porous, porosity coefficient, and weight fraction of BNNTs on maximum deflection and critical buckling load of the sandwich beam is studied. Although by increasing the temperature the stiffness of the beam should be decreased but due to the unique temperature properties of SMA, it's quite vice versa. When temperature increases (at fully austenite phase), the SMA molecular shape becomes more regular and their intermolecular forces enhance, that it leads to increase the critical buckling load and decreases maximum deflection. Also, due to the high thermal properties of SMA wires by increasing the volume fraction of SMA, the size of the heating/cooling cycle composed gets more and to this cause, the strength of the beam increases. Moreover, in the higher volume fraction of SMA, in the region of phase transformation from martensite to austenite the rate of increasing critical buckling load (decreasing maximum deflection) is more intensive. In this study, three different patterns of BNNTs contain uniform distribution, V-A and A-V distributions are considered. The results show that the type of V-A pattern among two other patterns has the highest critical buckling load and lowest maximum deflection and by contrast, the type of A-V pattern has the lowest buckling load and highest maximum deflection. As it is illustrated, by increasing the porosity coefficient the buckling load of sandwich Reddy beam with porous cored decreases and its deflection increases. And also, in the austenite phase, the stiffness of the beam is considerably more than its value in the martensite phase. It is noted that an increasing in the length to thickness ratio leads to a decrease of stiffness. As it can be observed, by increasing length-to-thickness, the critical buckling load decreases and maximum deflection increases. Also, three different distributions of porosity (symmetry, asymmetry and uniform) are investigated in this paper. As it is shown, the asymmetry porosity pattern provides the lowest stiffness among the other two patterns but by contrast, the symmetry distribution has the highest stiffness.

Acknowledgments

The authors would like to thank the referees for their valuable comments. Also, they are thankful to the Iranian Nanotechnology Development Committee for their financial support and the University of Kashan for supporting this work (Grant Number: 891238/6).

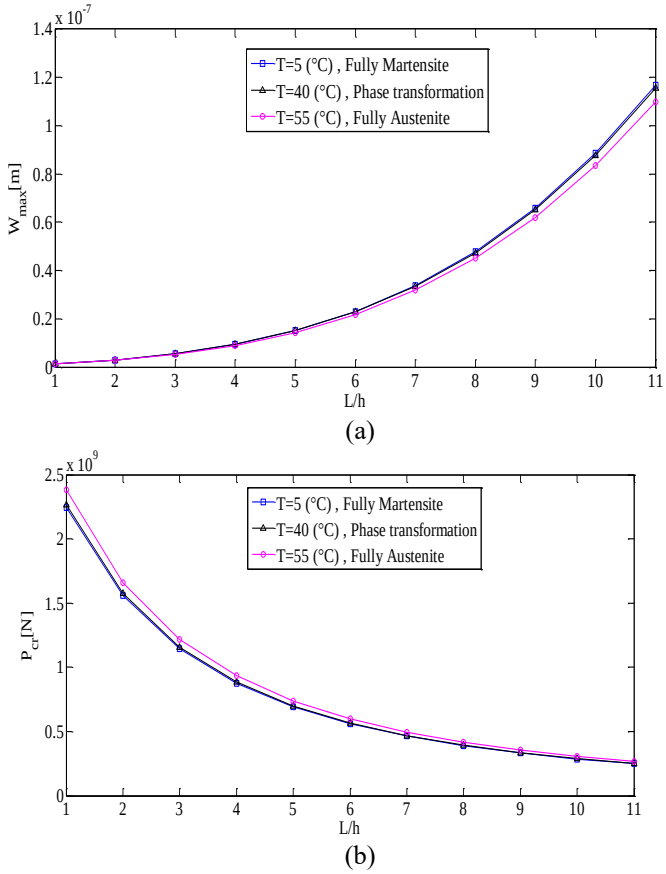

Fig. 9 The effect of length to thickness ratio in the various phases of SMA on (a) dimensional maximum deflection and (b) dimensional critical buckling load

References

Alambeigi K., Mohammadimehr M., Bamdad M. and Rabczuk, T. (2020), "Free and forced vibration analysis of a sandwich beam considering porous core and SMA hybrid composite face layers on Vlasov's foundation", *Acta Mechanica*, **231**, 3199-3218. https://doi.org/10.1007/s00707-020-02697-5.

Amiri, A., Mohammadimehr, M. and Anvari M. (2020), "Stress and buckling analysis of a thick-walled micro sandwich panel with a flexible foam core and carbon nanotube reinforced composite (CNTRC) face sheets", *Appl. Math. Mech.*, **41**(7), 1027-1038. https://doi.org/10.1007/s10483-020-2627-7.

Akbari, T. and Khalili, S.M.R. (2019), "Numerical simulation of buckling behavior of thin walled composite shells with embedded shape memory alloy wires", *Thin-Wall. Struct.*, **143**, 106193. https://doi.org/10.1016/j.tws.2019.106193.

Akhavan-Alavi, S.M., Mohammadimehr, M. and Edjtahed, S.H. (2019), "Active control of micro Reddy beam integrated with functionally graded nanocomposite sensor and actuator based on linear quadratic regulator method", *Eur. J. Mech.-A/Solids*, **74**, 449-461. https://doi.org/10.1016/j.euromechsol.2018.12.008.

Akhavan-Rad, B. and Kheirikhah, M.M. (2019), "Static analysis of sandwich plates embedded with shape memory alloy wires using active strain energy tuning method", *J. Brazilian Soc. Mech. Sci. Eng.*, **41**(3), 160. https://doi.org/10.1007/s40430-019-1666-2.

Arani, A.G., Arani, A.H.S. and Haghparast, E. (2018), "Bending analysis of magneto-electro-thermo-elastic functionally graded nano-beam based on first order shear deformation theory", *Int. J. Bio-Inorg. Hybr. Nanomater*, **7**(2), 163-176.

Arani, A.G., Pourjamshidian, M., Arefi, M. and Arani, M.R. (2019), "Thermal, electrical and mechanical buckling loads of sandwich nano-beams made of FG-CNTRC resting on Pasternak's foundation based on higher order shear deformation theory", *Struct. Eng. Mech.*, **69**(4), 439-455. https://doi.org/10.12989/sem.2019.69.4.439.

Arenal, R., Wang, M.S., Xu, Z., Loiseau, A. and Golberg, D. (2011), "Young modulus, mechanical and electrical properties of isolated individual and bundled single-walled boron nitride nanotubes", *Nanotechnology*, **22**(26), 265704. https://doi.org/10.1088/0957-4484/22/26/265704.

Babaeeian, M. and Mohammadimehr, M. (2020), "Investigation of the time elapsed effect on residual stress measurement in a composite plate by DIC method", *Opt. Lasers Eng.*, **128**. 106002. https://doi.org/10.1016/j.optlaseng.2020.106002

Babaee, A., Sadighi, M., Nikbakht, A. and Alimirzaei, S. (2018), "Generalized differential quadrature nonlinear buckling analysis of smart SMA/FG laminated beam resting on nonlinear elastic medium under thermal loading", *J. Therm. Stresses*, **41**(5), 583-607. https://doi.org/10.1080/01495739.2017.1408048.

Bamdad, M., Mohammadimehr, M. and Alambeigi, K. (2019), "Analysis of sandwich Timoshenko porous beam with temperature-dependent material properties: Magneto-electro-elastic vibration and buckling solution", *J. Vib. Control*, **25**(23-24), 2875-2893. https://doi.org/10.1177/1077546319860314.

Chaabane, L.A., Bourada, F., Sekkal, M., Zerouati, S., Zaoui, F.Z., Tounsi, A., Derras, A., Bousahla, A.A. and Tounsi, A. (2019), "Analytical study of bending and free vibration responses of functionally graded beams resting on elastic foundation", *Struct. Eng. Mech.*, **71**(2), 185-196.

https://doi.org/10.12989/sem.2019.71.2.185.

Chen, D., Kitipornchai, S. and Yang, J. (2016), "Nonlinear free vibration of shear deformable sandwich beam with a functionally graded porous core", *Thin-Wall. Struct.*, **107**, 39-48. https://doi.org/10.1016/j.tws.2016.05.025.

De Sousa, V. C., Tan, D., De Marqui Jr, C. and Erturk, A. (2018), "Tunable metamaterial beam with shape memory alloy resonators: Theory and experiment", *Appl. Phys. Lett.*, **113(**14), 143502. https://doi.org/10.1063/1.5050213.

Ebrahimi, F. and Barati, M.R. (2018), "Stability analysis of porous multi-phase nanocrystalline nonlocal beams based on a general higher-order couple-stress beam model", *Struct. Eng. Mech.*, **65**(4), 465-476. https://doi.org/10.12989/sem.2018.65.4.465.

Eltaher, M.A., Fouda, N., El-midany, T. and Sadoun, A.M. (2018), "Modified porosity model in analysis of functionally graded porous nanobeams", *J. Brazilian Soc. Mech. Sci. Eng.*, **40**(3), 141. https://doi.org/10.1007/s40430-018-1065-0.

Emdadi, M., Mohammadimehr, M. and Navi, B.R. (2019), "Free vibration of an annular sandwich plate with CNTRC facesheets and FG porous cores using Ritz method", *Adv. Nano Res.*, **7**(2), 109. https://doi.org/10.12989 /anr.2019.7.2.109.

Fang, W., Yu, T., Van Lich, L. and Bui, T.Q. (2019), "Analysis of thick porous beams by a quasi-3D theory and isogeometric analysis", *Compos. Struct.*, **221**, 110890. https://doi.org/10.1016/j.compstruct.2019.04.062.

Faraji-Oskouie, M., Norouzzadeh, A., Ansari, R. and Rouhi, H. (2019), "Bending of small-scale Timoshenko beams based on the integral/differential nonlocal-micropolar elasticity theory: a finite element approach", *Appl. Math. Mech.*, **40**(6), 767-782. https://doi.org/10.1007/s10483-019-2491-9.

He, Y., Li, Y., Liu, Z. and Liew, K.M. (2017), "Buckling analysis and buckling control of thin films on shape memory polymer substrate", *Eur. J. Mech.-A/Solids*, **66**, 356-369. https://doi.org/10.1016/j.euromechsol.2017.08.006.

Heydari, A. and Shariati, M. (2018), "Buckling analysis of tapered BDFGM nano-beam under variable axial compression resting on elastic medium", *Struct. Eng. Mech.*, **66**(6), 737-748. https://doi.org/10.12989/sem.2018.66.6.737.

Huang, Y., Lin, J., Tang, C., Bando, Y., Zhi, C., Zhai, T., Dierre, B., Sekiguchi, T. and Golberg, D. (2011), "Bulk synthesis, growth mechanism and properties of highly pure ultrafine boron nitride nanotubes with diameters of sub-10 nm", *Nanotechnology*, **22**(14), 145602. https://doi.org/10.1088/0957-4484/22/14/145602.

Kabir, M.Z. and Tehrani, B.T. (2017), "Closed-form solution for thermal, mechanical, and thermo-mechanical buckling and post-buckling of SMA composite plates", *Compos. Struct.*, **168**, 535-548. https://doi.org/10.1016/j.compstruct.2017.02.046.

Kaci, A., Houari, M.S.A., Bousahla, A.A., Tounsi, A. and Mahmoud, S.R. (2018), "Post-buckling analysis of shear-deformable composite beams using a novel simple two-unknown beam theory", *Struct. Eng. Mech.*, **65**(5), 621-631. https://doi.org/10.12989/sem.2018.65.5.621.

Kheirikhah, M.M. and Khosravi, P. (2018), "Buckling and free vibration analyses of composite sandwich plates reinforced by shape-memory alloy wires", *J. Brazilian Soc. Mech. Sci. Eng.*, **40**(11), 515. https://doi.org/10.1007/s40430-018-1438-4.

Kozikowska, A. (2019), "Multi-objective topology and geometry optimization of statically determinate beams", *Struct. Eng. Mech.*, **70**(3), 367-380. https://doi.org/10.12989/sem.2019.70.3.367.

Lee, J.W. and Lee, J.Y. (2018), "A transfer matrix method for in-plane bending vibrations of tapered beams with axial force and multiple edge cracks", *Struct. Eng. Mech.*, **66**(1), 125-138. https://doi.org/10.12989/sem.2018.66.1.125.

Liu, Y., Su, S., Huang, H. and Liang, Y. (2019), "Thermal-mechanical coupling buckling analysis of porous functionally graded sandwich beams based on physical neutral plane", *Compos. Part B: Eng.*, **168**, 236-242. https://doi.org/10.1016/j.compositesb.2018.12.063.

Mohammadimehr, M., Atifeh, S.J. and Rousta Navi, B. (2018a), "Stress and free vibration analysis of piezoelectric hollow circular FG-SWBNNTs reinforced nanocomposite plate based on modified couple stress theory subjected to thermo-mechanical loadings", *J. Vib. Control*, **24**(15), 3471-3486. https://doi.org/10.1177/1077546317706887.

Mohammadimehr, M., Mohammadi-Dehabadi, A.A., Akhavan Alavi, S.M., Alambeigi, K., Bamdad, M., Yazdani, R. and Hanifehlou, S. (2018b), "Bending, buckling, and free vibration analyses of carbon nanotube reinforced composite beams and experimental tensile test to obtain the mechanical properties of nanocomposite", *Steel Compos. Struct.*, **29**(3), 405-422. https://doi.org/10.12989/scs.2018.29.3.405.

Mohammadimehr, M. and Rostami, R. (2018), "Bending and vibration analyses of a rotating sandwich cylindrical shell considering nanocomposite core and piezoelectric layers subjected to thermal and magnetic fields", *Appl. Math. Mech.*, **39**(2). 219-240, https://doi.org/10.1007/s10483-018-2301-6.

Nguyen, N.D., Nguyen, T.K., Vo, T.P., Nguyen, T.N. and Lee, S. (2019), "Vibration and buckling behaviours of thin-walled composite and functionally graded sandwich I-beams", *Compos. Part B: Eng.*, **166**, 414-427. https://doi.org/10.1016/j.compositesb.2019.02.033.

Polit, O., Anant, C., Anirudh, B. and Ganapathi, M. (2019), "Functionally graded graphene reinforced porous nanocomposite curved beams: Bending and elastic stability using a higher-order model with thickness stretch effect", *Compos. Part B: Eng.*, **166**, 310-327. https://doi.org/10.1016/j.compositesb.2018.11.074.

Rafiee, M.A., Rafiee, J., Wang, Z., Song, H., Yu, Z.Z. and Koratkar, N. (2009), "Enhanced mechanical properties of nanocomposites at low graphene content", *ACS Nano*, **3**(12), 3884-3890. https://doi.org/10.1021/nn9010472.

Rajabi, J. and Mohammadimehr, M. (2019), "Bending analysis of a micro sandwich skew plate using extended Kantorovich method based on Eshelby-Mori-Tanaka approach", *Comput. Concrete*, **23**(5), 361-376. https://doi.org/10.12989/cac.2019.23.5.361.

Sahmani, S., Aghdam, M.M. and Rabczuk, T. (2018), "Nonlinear bending of functionally graded porous micro/nano-beams reinforced with graphene platelets based upon nonlocal strain gradient theory", *Compos. Struct.*, **186**, 68-78. https://doi.org/10.1016/j.compstruct.2017.11.082.

Soltanieh, G., Kabir, M.Z. and Shariyat, M. (2019), "Improvement of the dynamic instability of shallow hybrid composite cylindrical shells under impulse loads using shape memory alloy wires", *Compos.Part B: Eng.*, **167**, 167-179. https://doi.org/10.1016/j.compositesb.2018.12.040.

Tang, H., Li, L. and Hu, Y. (2018), "Buckling analysis of two-directionally porous beam", *Aerosp. Sci. Technol.*, **78**, 471-479. https://doi.org/10.1016/j.ast.2018.04.045.

Thai, H.T. and Vo, T.P. (2012), "Bending and free vibration of functionally graded beams using various higher-order shear deformation beam theories", *Int. J. Mech. Sci.*, **62**(1), 57-66. https://doi.org/10.1016/j.ijmecsci.2012.05.014.

Thanh, C.L., Tran, L.V., Bui, T.Q., Nguyen, H.X. and Abdel-Wahab, M. (2019), "Isogeometric analysis for size-dependent nonlinear thermal stability of porous FG microplates", *Compos. Struct.*, **221**, 110838. https://doi.org/10.1016/j.compstruct.2019.04.010.

Wang, C.M., Reddy, J.N. and Lee, K.H. (Eds.) (2000), "Shear deformable beams and plates: Relationships with classical solutions", Elsevier.

Wattanasakulpong, N. and Bui, T.Q. (2018), "Vibration analysis of

third-order shear deformable FGM beams with elastic support by Chebyshev collocation method", *Int. J. Struct. Stab. Dynam.*, **18**(5), 1850071. https://doi.org/10.1142/S0219455418500712.

Wu, H., Kitipornchai, S. and Yang, J. (2015), "Free vibration and buckling analysis of sandwich beams with functionally graded carbon nanotube-reinforced composite face sheets", *Int. J. Struct. Stab. Dynam.*, **15**(7), 1540011. https://doi.org/10.1142/S0219455415400118.

Yazdani, R., Mohammadimehr, M. and Navi, B.R. (2019), "Free vibration of Cooper-Naghdi micro saturated porous sandwich cylindrical shells with reinforced CNT face sheets under magneto-hydro-thermo-mechanical loadings", *Struct. Eng. Mech.*, **70**(3), 351-365. https://doi.org/10.12989/sem.2019.70.3.351.

Yu, C., Kang, G. and Kan, Q. (2018), "A micromechanical constitutive model for grain size dependent thermo-mechanically coupled inelastic deformation of super-elastic NiTi shape memory alloy", *Int. J.Plasticity*, **105**, 99-127. https://doi.org/10.1016/j.ijplas.2018.02.005.

CC

Appendix

As illustrated in Fig. 9 increase the length to thickness ratio the dimensional critical buckling load is decreased and the dimensional maximum deflection is increased.

7.1 A

$$\mathrm{V_{BNNT}}=\begin{cases}\mathrm{V^{t}_{BNNT}}=\dfrac{2\mathrm{z}-\mathrm{h_c}}{\mathrm{h_f}}\mathrm{V^{*}}\\ \mathrm{V^{b}_{BNNT}}=\dfrac{2\mathrm{z}+\mathrm{h_c}}{-\mathrm{h_f}}\mathrm{V^{*}}\end{cases}\qquad \text{pattern: V}-\text{A}$$

$$\mathrm{V_{BNNT}}=\begin{cases}\mathrm{V^{t}_{BNNT}}=\mathrm{V^{*}}\\ \mathrm{V^{b}_{BNNT}}=\mathrm{V^{*}}\end{cases}\qquad \text{pattern: Uniform}$$

$$\mathrm{V_{BNNT}}=\begin{cases}\mathrm{V^{t}_{BNNT}}=\dfrac{\mathrm{h_c}+2\mathrm{h_f}-2\mathrm{z}}{\mathrm{h_f}}\mathrm{V^{*}}\\ \mathrm{V^{b}_{BNNT}}=\dfrac{\mathrm{h_c}+2\mathrm{h_f}+2\mathrm{z}}{\mathrm{h_f}}\mathrm{V^{*}}\end{cases}\qquad \text{pattern: A}-\text{V}$$

$$V^{*}=\frac{W_{BNNT}}{\left(\left(\rho_{BNNT}/\rho_{epoxy}\right)-\left(\rho_{BNNT}/\rho_{epoxy}\right)W_{BNNT}+W_{BNNT}\right)}$$

Subscripts "*t*" and "*b*" denotes the top and bottom layers [31].

7.2 B

Three type dispersion are given here Bamdad *et al.* (2019)

$$\psi(z)=\begin{cases}\cos\left(\dfrac{\pi\mathrm{z}}{\mathrm{h_c}}\right) & \rightarrow \text{ Symmetry}\\ \cos\left(\dfrac{\pi\mathrm{z}}{2\mathrm{h}_c}+\dfrac{\pi}{4}\right) & \rightarrow \text{Asymmetry}\\ \psi & \rightarrow \text{ Uniform}\end{cases}$$

$$\lambda(\mathrm{z})=\begin{cases}1-\mathrm{e_m}\psi(z) & \text{Symmetry , Asymmetry}\\ \sqrt{1-\mathrm{e_0}\psi} & \text{Uniform}\end{cases}$$

$$\psi=\frac{1}{\mathrm{e_0}}-\frac{1}{\mathrm{e_0}}\left(\frac{2}{\pi}\sqrt{1-\mathrm{e_0}}-\frac{2}{\pi}+1\right)^{2},\qquad \mathrm{e_m}=1-\sqrt{1-\mathrm{e_0}}$$

7.3 C

$$\begin{cases}\varepsilon^{i}_{xx}=\dfrac{\partial u^{i}(x,z)}{\partial \mathrm{x}}=\dfrac{\mathrm{d}u^{i}_{0}(x)}{\mathrm{dx}}+z\dfrac{\mathrm{d}\emptyset^{i}(x)}{\mathrm{dx}}-\dfrac{4z^{3}}{3h_{i}^{2}}\left(\dfrac{\mathrm{d}\emptyset^{i}(x)}{\mathrm{dx}}+\dfrac{d^{2}w^{i}_{0}(x)}{dx^{2}}\right)\\ \gamma^{i}_{xz}=\dfrac{\partial u^{i}(x,z)}{\partial \mathrm{z}}+\dfrac{\partial w^{i}(x,z)}{\partial \mathrm{x}}=\emptyset^{i}(x)-\dfrac{4z^{2}}{h_{i}^{2}}\left(\emptyset^{i}(x)+\dfrac{dw^{i}_{0}(x)}{dx}\right)+\dfrac{dw^{i}_{0}(x)}{dx}\end{cases}$$

7.4 D

$$Q_{11}=\frac{E_m}{1-{\nu_m}^{2}}$$

$$Q_{55}=G_m=\frac{E_m}{2(1+\nu_m)}$$

$$C_{11}=\frac{E_c(z)}{1-\nu_c(z)^{2}}$$

$$C_{55}=G_c=\frac{E_c}{2(1+\nu_c)}$$

7.5 E

$$D_{11}=\frac{E_f(\rho)}{1-\nu_f(\rho)^{2}}$$

$$D_{12}=D_{21}=\frac{E_f(\rho)\nu_f(\rho)}{1-\nu_f(\rho)^{2}}$$

$$D_{55}=G_f=\frac{E_f(\rho)}{2(1+\nu_f(\rho))}$$

Subscript "*f*" denotes the foundation.

7.6 F

$$\begin{aligned}\boldsymbol{\delta u_0}:\ &-2\frac{\partial}{\partial x}u(x)T\theta+2\frac{\partial}{\partial x}u(x)T_0\theta+\frac{4}{3}\frac{\frac{\partial^3}{\partial x^3}w(x)}{{h_{bf}}^{2}}ubf_{113}+\frac{4}{3}\frac{\frac{\partial^3}{\partial x^3}w(x)}{{h_{tf}}^{2}}utf_{113}+\\ &\frac{4}{3}\frac{\frac{\partial^2}{\partial x^2}\phi(x)}{{h_{bf}}^{2}}ubf_{113}+\frac{4}{3}\frac{\frac{\partial^2}{\partial x^2}\phi(x)}{{h_{tf}}^{2}}utf_{113}\\ &+\frac{4}{3}\frac{\frac{\partial^2}{\partial x^2}\phi(x)}{{h_c}^{2}}uc_{113}-\frac{\partial^2}{\partial x^2}u(x)ubf_{110}+\frac{4}{3}\frac{\frac{\partial^3}{\partial x^3}w(x)}{{h_c}^{2}}uc_{113}-\frac{\partial^2}{\partial x^2}\phi(x)ubf_{111}\\ &-\frac{\partial^2}{\partial x^2}\phi(x)utf_{111}-\frac{\partial^2}{\partial x^2}u(x)utf_{110}-\frac{\partial^2}{\partial x^2}\phi(x)uc_{111}-\frac{\partial^2}{\partial x^2}u(x)uc_{110}+\\ &2\frac{\partial}{\partial x}u(x)\xi_s\varepsilon_L\xi=0\end{aligned}$$

$$\begin{aligned}\boldsymbol{\delta w_0}:\ &\frac{8\frac{\partial}{\partial x}\phi(x)}{{h_{bf}}^{2}}ubf_{552}-\frac{16\frac{\partial}{\partial x}\phi(x)}{{h_c}^{4}}uc_{554}+\frac{8\frac{\partial}{\partial x}\phi(x)}{{h_c}^{2}}uc_{552}\\ &-\frac{16\frac{\partial}{\partial x}\phi(x)}{{h_{tf}}^{4}}utf_{554}\\ &-\frac{16\frac{\partial}{\partial x}\phi(x)}{{h_{bf}}^{4}}ubf_{554}-\frac{16\frac{\partial^2}{\partial x^2}w(x)}{{h_c}^{4}}uc_{554}+\frac{16}{9}\frac{\frac{\partial^4}{\partial x^4}w(x)}{{h_c}^{4}}uc_{116}\\ &-\frac{4}{3}\frac{\frac{\partial^3}{\partial x^3}\phi(x)}{{h_c}^{2}}uc_{114}\\ &+\frac{8\frac{\partial^2}{\partial x^2}w(x)}{{h_c}^{2}}uc_{552}-\frac{\partial^2}{\partial x^2}w(x)N_x+\frac{16}{9}\frac{\frac{\partial^4}{\partial x^4}w(x)}{{h_{tf}}^{4}}utf_{116}\\ &+\frac{16}{9}\frac{\frac{\partial^3}{\partial x^3}\phi(x)}{{h_{bf}}^{4}}ubf_{116}\\ &-\frac{4}{3}\frac{\frac{\partial^3}{\partial x^3}u(x)}{{h_{bf}}^{2}}ubf_{113}+\frac{16}{9}\frac{\frac{\partial^3}{\partial x^3}\phi(x)}{{h_{tf}}^{4}}utf_{116}+\frac{16}{9}\frac{\frac{\partial^3}{\partial x^3}\phi(x)}{{h_{bf}}^{4}}ubf_{116}\\ &-\frac{4}{3}\frac{\frac{\partial^3}{\partial x^3}\phi(x)}{{h_{bf}}^{2}}ubf_{114}\\ &-\frac{4}{3}\frac{\frac{\partial^3}{\partial x^3}\phi(x)}{{h_{tf}}^{2}}utf_{114}+\frac{8\frac{\partial^2}{\partial x^2}w(x)}{{h_{tf}}^{2}}utf_{552}+\frac{8\frac{\partial^2}{\partial x^2}w(x)}{{h_{bf}}^{2}}ubf_{552}\\ &-\frac{16\frac{\partial^2}{\partial x^2}w(x)}{{h_{tf}}^{4}}utf_{554}\\ &-\frac{16\frac{\partial^2}{\partial x^2}w(x)}{{h_{bf}}^{4}}ubf_{554}+\frac{16}{9}\frac{\frac{\partial^4}{\partial x^4}w(x)}{{h_{bf}}^{4}}ubf_{116}-\frac{4}{3}\frac{\frac{\partial^3}{\partial x^3}u(x)}{{h_{tf}}^{2}}utf_{113}\\ &-\frac{\partial}{\partial x}\phi(x)utf_{550}\\ &-\frac{\partial}{\partial x}\phi(x)ubf_{550}-\frac{\partial}{\partial x}\phi(x)uc_{550}+\frac{16}{9}\frac{\frac{\partial^3}{\partial x^3}\phi(x)}{{h_c}^{4}}uc_{116}\\ &-\frac{4}{3}\frac{\frac{\partial^3}{\partial x^3}u(x)}{{h_c}^{2}}uc_{113}+q(x)\end{aligned}$$

$$-\frac{\partial^2}{\partial x^2}w(x)ubf_{550}-\frac{\partial^2}{\partial x^2}w(x)uc_{550}-\frac{\partial^2}{\partial x^2}w(x)utf_{550}+K_w w(x)-K_s\frac{\partial^2}{\partial x^2}w(x)+\frac{8\frac{\partial}{\partial x}\phi(x)}{{h_{tf}}^2}utf_{552}-\frac{4\frac{\partial^2}{\partial x^2}w(x)}{{h_{bf}}^2}T\theta usb_3+\frac{4\frac{\partial^2}{\partial x^2}w(x)}{{h_{tf}}^2}T_0\theta ust_3-\frac{4\frac{\partial^2}{\partial x^2}w(x)}{{h_{tf}}^2}T\theta ust_3+\frac{4\frac{\partial^2}{\partial x^2}w(x)}{{h_{tf}}^2}\xi_s\varepsilon_L\xi ust_3+\frac{4\frac{\partial^2}{\partial x^2}w(x)}{{h_{bf}}^2}\xi_s\varepsilon_L\xi usb_3=0$$

$$\boldsymbol{\delta\phi}:-\frac{4\frac{\partial}{\partial x}\phi(x)}{{h_{bf}}^2}\xi_s\varepsilon_L\xi usb_3-\frac{4\frac{\partial}{\partial x}\phi(x)}{{h_{tf}}^2}\xi_s\varepsilon_L\xi ust_3+\frac{\partial}{\partial x}w(x)uc_{550}+\phi(x)uc_{550}+\frac{16\phi(x)}{{h_c}^4}uc_{554}-\frac{8\phi(x)}{{h_c}^2}uc_{552}-\frac{8\frac{\partial}{\partial x}w(x)}{{h_c}^2}uc_{552}+\frac{16\frac{\partial}{\partial x}w(x)}{{h_{tf}}^4}utf_{554}-\frac{8\phi(x)}{{h_{tf}}^2}utf_{552}-\frac{8\frac{\partial}{\partial x}w(x)}{{h_{tf}}^2}utf_{552}+\frac{16\frac{\partial}{\partial x}w(x)}{{h_{bf}}^4}ubf_{554}+\frac{16\phi(x)}{{h_{bf}}^4}ubf_{554}+\frac{16\phi(x)}{{h_{tf}}^4}utf_{554}+\frac{16\frac{\partial}{\partial x}w(x)}{{h_c}^4}uc_{554}-\frac{8\phi(x)}{{h_{bf}}^2}ubf_{552}-\frac{8\frac{\partial}{\partial x}w(x)}{{h_{bf}}^2}ubf_{552}-\frac{16}{9}\frac{\partial^2}{\partial x^2}\frac{\phi(x)}{{h_{tf}}^4}utf_{116}+\frac{4}{3}\frac{\partial^2}{\partial x^2}\frac{u(x)}{{h_{bf}}^2}ubf_{113}+\frac{4}{3}\frac{\partial^3}{\partial x^3}\frac{w(x)}{{h_{bf}}^2}ubf_{114}-\frac{16}{9}\frac{\partial^3}{\partial x^3}\frac{w(x)}{{h_{bf}}^4}ubf_{116}+\frac{4}{3}\frac{\partial^3}{\partial x^3}\frac{w(x)}{{h_{tf}}^2}utf_{114}+\frac{4}{3}\frac{\partial^2}{\partial x^2}\frac{u(x)}{{h_c}^2}uc_{113}-\frac{16}{9}\frac{\partial^2}{\partial x^2}\frac{\phi(x)}{{h_c}^4}uc_{116}-\frac{16}{9}\frac{\partial^3}{\partial x^3}\frac{w(x)}{{h_c}^4}uc_{116}-\frac{16}{9}\frac{\partial^2}{\partial x^2}\frac{\phi(x)}{{h_{bf}}^4}ubf_{116}+\frac{8}{3}\frac{\partial^2}{\partial x^2}\frac{\phi(x)}{{h_c}^2}uc_{116}+\frac{4}{3}\frac{\partial^3}{\partial x^3}\frac{w(x)}{{h_c}^2}uc_{114}+\frac{8}{3}\frac{\partial^2}{\partial x^2}\frac{\phi(x)}{{h_{bf}}^2}ubf_{116}-\frac{16}{9}\frac{\partial^3}{\partial x^3}\frac{w(x)}{{h_{tf}}^4}utf_{116}+\frac{4}{3}\frac{\partial^2}{\partial x^2}\frac{u(x)}{{h_{tf}}^2}utf_{114}+\frac{8}{3}\frac{\partial^2}{\partial x^2}\frac{\phi(x)}{{h_{tf}}^2}utf_{116}+\frac{\partial}{\partial x}w(x)ubf_{550}+\phi(x)ubf_{550}+\phi(x)utf_{550}$$

$$\frac{\partial}{\partial x}w(x)utf_{550}-\frac{4\frac{\partial}{\partial x}\phi(x)}{{h_{tf}}^2}T_0\theta ust_3+\frac{\partial}{\partial x}\phi(x)T_0\theta usb_1-\frac{\partial^2}{\partial x^2}\phi(x)uc_{112}-\frac{\partial}{\partial x}\phi(x)T\theta usb_1+\frac{4}{3}\frac{\partial}{\partial x}\frac{\phi(x)}{{h_{bf}}^2}T\theta usb_3-\frac{4}{3}\frac{\partial}{\partial x}\frac{\phi(x)}{{h_{bf}}^2}T_0\theta usb_3+\frac{\partial}{\partial x}\phi(x)\xi_s\varepsilon_L\xi ust_1-\frac{\partial}{\partial x}\phi(x)T\theta ust_1+\frac{4}{3}\frac{\partial}{\partial x}\frac{\phi(x)}{{h_{tf}}^2}T\theta ust_3+\frac{\partial}{\partial x}\phi(x)\xi_s\varepsilon_L\xi usb_1-\frac{\partial^2}{\partial x^2}u(x)uc_{111}-\frac{\partial^2}{\partial x^2}\phi(x)utf_{112}-\frac{\partial^2}{\partial x^2}\phi(x)ubf_{112}-\frac{\partial^2}{\partial x^2}u(x)ubf_{111}-\frac{\partial^2}{\partial x^2}u(x)utf_{111}+\frac{\partial}{\partial x}\phi(x)T_0\theta ust_1=$$

$$uc_{111}=\int_{-h_c/2}^{h_c/2}C_{11}(z)\times z dz$$

$$uc_{113}=\int_{-h_c/2}^{h_c/2}C_{11}(z)\times z^3 dz$$

$$uc_{116}=\int_{-h_c/2}^{h_c/2}C_{11}(z)\times z^6 dz$$

$$uc_{552}=\int_{-h_c/2}^{h_c/2}C_{11}(z)\times z^5 dz$$

$$ubf_{110}=\int_{-\frac{h_c}{2}-h_f}^{-h_c/2}Q_{11}(z)dz$$

$$ubf_{112}=\int_{-\frac{h_c}{2}-h_f}^{-h_c/2}Q_{11}(z)\times z^2 dz$$

$$ubf_{114}=\int_{-\frac{h_c}{2}-h_f}^{-h_c/2}Q_{11}(z)\times z^4 dz$$

$$ubf_{550}=\int_{-\frac{h_c}{2}-h_f}^{-h_c/2}Q_{55}(z)dz$$

$$ubf_{554}=\int_{-\frac{h_c}{2}-h_f}^{-h_c/2}Q_{55}(z)\times z^4 dz$$

$$utf_{111}=\int_{\frac{h_c}{2}}^{\frac{h_c}{2}+h_f}Q_{11}(z)\times z\ \ dz$$

$$utf_{113}=\int_{\frac{h_c}{2}}^{\frac{h_c}{2}+h_f}Q_{11}(z)\times z^3 dz$$

$$utf_{116}=\int_{\frac{h_c}{2}}^{\frac{h_c}{2}+h_f}Q_{11}(z)\times z^6 dz$$

$$utf_{552}=\int_{\frac{h_c}{2}}^{\frac{h_c}{2}+h_f}Q_{55}(z)\times z^2 dz$$

$$uc_{110}=\int_{-h_c/2}^{h_c/2}C_{11}(z)dz$$

$$uc_{112}=\int_{-h_c/2}^{h_c/2}C_{11}(z)\times z^2 dz$$

$$uc_{114}=\int_{-h_c/2}^{h_c/2}C_{11}(z)\times z^4 dz$$

$$uc_{550} = \int_{-h_c/2}^{h_c/2} C_{55}(z)dz$$

$$uc_{554} = \int_{-h_c/2}^{h_c/2} C_{55}(z) \times z^4 dz$$

$$ubf_{111} = \int_{-\frac{h_c}{2}-h_f}^{-h_c/2} Q_{11}(z) \times z \quad dz$$

$$ubf_{113} = \int_{-\frac{h_c}{2}-h_f}^{-h_c/2} Q_{11}(z) \times z^3 dz$$

$$ubf_{116} = \int_{-\frac{h_c}{2}-h_f}^{-h_c/2} Q_{11}(z) \times z^6 dz$$

$$ubf_{552} = \int_{-\frac{h_c}{2}-h_f}^{-h_c/2} Q_{55}(z) \times z^2 dz$$

$$utf_{110} = \int_{\frac{h_c}{2}}^{\frac{h_c}{2}+h_f} Q_{11}(z)dz$$

$$utf_{112} = \int_{\frac{h_c}{2}}^{\frac{h_c}{2}+h_f} Q_{11}(z) \times z^2 dz$$

$$utf_{114} = \int_{\frac{h_c}{2}}^{\frac{h_c}{2}+h_f} Q_{11}(z) \times z^4 dz$$

$$utf_{550} = \int_{\frac{h_c}{2}}^{\frac{h_c}{2}+h_f} Q_{55}(z)dz$$

$$utf_{554} = \int_{\frac{h_c}{2}}^{\frac{h_c}{2}+h_f} Q_{55}(z) \times z^4 dz$$